

Anisotropic Defect Diffusion in Layered $\text{CsPbBr}_x\text{I}_{3-x}$ Perovskites

Konrad Wilke,[†] Mike Pols,[†] Titus S. van Erp,[‡] Geert Brocks,[¶] and Shuxia Tao^{*,†}

[†]*Department of Applied Physics and Science Education, Eindhoven University of Technology, 5600 MB, Eindhoven, The Netherlands*

[‡]*Department of Chemistry and Biomedical Science, Norwegian University of Science and Technology, 7941 Trondheim, Norway*

[¶]*Department of Applied Physics and Science Education, Eindhoven University of Technology, 5600 MB, Eindhoven, The Netherlands; Computational Chemical Physics, Faculty of Science and Technology and MESA+ Institute for Nanotechnology, University of Twente, Enschede 7500 AE, The Netherlands.*

E-mail: s.x.tao@tue.nl

Abstract

Mixed-halide perovskites offer a route to enhance phase stability and modify optoelectronic properties. Here, we use large-scale molecular dynamics simulations with a reactive force field to investigate defects in $\text{CsPbBr}_x\text{I}_{3-x}$ perovskites, focusing on how defect mobility can be controlled and the stability of the material may be improved by layered ordering of Br and I anions in layers. Our results show that layered halide ordering induces strongly anisotropic defect diffusion: migration proceeds readily along the layers, whereas diffusion across them is strongly suppressed. For Cs defects, this anisotropy originates from directional lattice strain and the associated octahedral tilting, while halide migration is governed by an interplay between strain and preferential local halide bonding configurations.

Keywords

Halide perovskites, defects, diffusion, migration, reactive force field, ion migration, strain engineering, ordering, stability, optoelectronics

1 Introduction

Metal halide perovskites (MHPs) with general formula ABX_3 (A = monovalent cation, B = metal, X = halide) have revolutionized optoelectronics due to their tunable band gaps,¹⁻³ high carrier mobilities,⁴⁻⁶ and low-cost processability.⁷⁻⁹ Extensive research over the past two decades has resulted in power conversion efficiencies exceeding 26% in photovoltaic applications,^{10,11} yet challenges remain regarding structural stability.¹²⁻¹⁶

All-inorganic halide perovskites, CsPbX_3 (X = Cl, Br, I) in particular, offer improved thermal stability relative to their organic-inorganic counterparts, as they do not suffer from the decomposition reactions that affect organic molecules such as methylammonium (MA).^{17,18} The 1.73 eV band gap of CsPbI_3 ¹⁹ is relatively close to the optimal value of 1.34 eV required for the Shockley-Queisser limit for photovoltaic efficiency.²⁰ However, the photoactive black perovskite phase of CsPbI_3 is only metastable at room temperature, and susceptible to a phase transition to the more stable non-perovskite yellow δ -phase.²¹⁻²⁵

The black phase can be stabilized by replacing part of the I by Br ions, thereby improving the size compatibility of the ions in the lattice, in accordance with the Goldschmidt tolerance factor.^{26,27}

Unfortunately, the band gap then also becomes larger (with CsPbBr₃ having a band gap of 2.37 eV),²⁸ and thus the material becomes less suitable for single-junction solar cells.^{15,29}

A strategy to alleviate this could be a layered halide ordering, which in case of CsPbBr₂I reduces the band gap by up to 0.2 eV in comparison to a random alloy.³⁰ The main idea is that ordering halide ions of different size introduces anisotropy in the strain field.³¹ This limits the octahedral tilting of the PbX₆ octahedrons, which is predicted to reduce the band gap.^{30,32}

Deng et al. recently demonstrated a realization of layered halide orderings in CsPbBr_xI_{3-x} through solvent evaporation via the antisolvent protection method.³⁰ With the same method Lin et al. obtained ordered DMAPbBr_xI_{3-x} (DMA = dimethylammonium) single crystals as precursors for layer-ordered CsPbBr_xI_{3-x} thin films.³³ Such ordering reduces the band gap and leads to increased carrier mobility.^{30,33}

Interestingly, besides the ability to tune optoelectronic properties, halide ordering can also increase the stability of CsPbBr_xI_{3-x} perovskite phase beyond what would be expected on the basis of the Goldschmidt tolerance factor.³⁰ A contributing factor could again be the anisotropic strain field. Indeed, a stabilizing influence of biaxial strain on CsPbI₃ and CsPbBr_xI_{3-x} ($x \leq 0.1$) has been reported experimentally, and ascribed to a lowering of the energy difference between the metastable black phase and the yellow phase.³⁴

Besides the thermodynamic effect of strain, there may also be an effect on the kinetics of degradation. Lattice point defects, such as vacancies and interstitials, can play a pivotal role in destabilizing halide perovskite phases.^{15,26,35-38} For example, Pols et al. demonstrated that iodine vacancies are very mobile and act as degradation initiators.³⁵ Delugas et al. observed anisotropic halide defect migration and suggested attempting to control it with strain and composition.³⁶

In this paper, we explore ordering the halide species in CsPbBr_xI_{3-x} to steer the migration of point defects, and effectively block it in certain directions. We investigate the directional defect diffusion in CsPbBr_xI_{3-x} perovskites by means of molecular dynamics (MD) simulations. We consider the motion of anion vacancies and intersti-

tials of Br and I, but also that of Cs cation defects, which we show have a comparable mobility. By comparing layered and randomly mixed halide orderings, we disentangle the effects on defect behavior of chemical heterogeneity from strain-induced structural distortions. To isolate the influence of lattice strain alone, we apply controlled biaxial strain to pure α -CsPbI₃ and α -CsPbBr₃ structures.

This approach allows us to systematically probe how both chemical composition and mechanical strain govern defect energetics and migration pathways and dynamics. Our study offers atomistic insight of strain engineering into defect-mediated transport in layered halide perovskites. It informs design strategies to optimize ionic and electronic properties for high-performance optoelectronic applications.

2 Computational Methods

2.1 Structural Models

To study effects of layered halide ordering on the migration of defects and the structure of CsPbBr_xI_{3-x}, we focus on the ordered (od-)CsPbBr₂I compound (Fig. 1 a) - c)) synthesized in Ref. 30. For comparison, we also consider the iodine-rich, ordered counterpart od-CsPbBrI₂ (Fig. 1 d) - f)) and the corresponding structures with unordered (ud) halides: ud-CsPbBr₂I and ud-CsPbBrI₂. In the od-structures, the majority halide ions fill all sites on every other Pb-X layer and the neighboring Cs-X layers, and the minority halide ions fill the remaining Pb-X layers, see Fig. 1. We compare results obtained with these ordered structures with results obtained with random structures of the same composition.

We construct 4x4x4 supercells of the primitive cubic cell of the high temperature phases of CsPbI₃ and CsPbBr₃: α -CsPbI₃ and α -CsPbBr₃ (space group Pm $\bar{3}$ m) with 320 atoms. The ordered structures are constructed as explained above; the randomly mixed structures are generated by randomly positioning I and Br on halide positions, so that the Br:I ratio is maintained in all space directions. Defective systems are created by placing a single I or Br vacancy or interstitial,

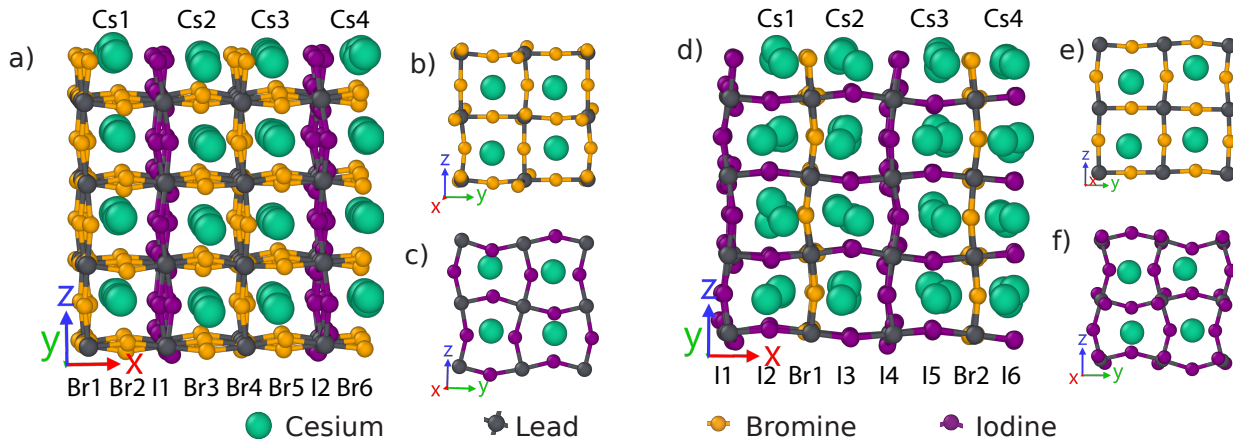


Figure 1: a) Supercell of od-CsPbBr₂I with Br and I layers stacked along the x-direction; b), c) top views of Br and I layers. d), e), f), similar for od-CsPbBr₂.

or a Cs vacancy or interstitial, inside the supercell.

2.2 Molecular dynamics simulations

Several high-quality force fields have been created to describe the ion dynamics in CsPbI₃, based either on the reactive force field (ReaxFF) model,³⁵ or on on-the-fly machine-learned force fields (MLFFs).^{39,40} Recently, a ReaxFF force field has been constructed that is capable of describing mixed halide systems CsPbBr_xI_{3-x},⁴¹ as well as an MLFF based on a neural network potential for the same purpose.⁴² In the present study we utilize the ReaxFF force field of Pols et al.⁴¹ for its competitive speed and robust description of the variety of complex environments. This allows us to extend the atomistic simulations towards large time scales.

All molecular dynamics (MD) simulations have been carried out in AMS2024.⁴³ The simulations were performed at 700 K, with a time step of 0.25 fs and an output frequency of 0.1 ps. Production runs were prepared with an *NVT*-equilibration of 50 ps and a Berendsen thermostat⁴⁴ with damping constant $\tau_T = 100$ fs, which was also applied in all further runs. The atomic positions were taken from the last frame of the respective equilibration. The production runs used a Nose-Hoover-Chain thermostat⁴⁵ with a chain length of 10. The production runs were carried out for 10 ns in the *NVT*-ensemble, with an out-

put frequency of 0.5 ps.

The volume of the supercell was determined in a simulation of the defect-free system. For that simulation, the equilibration was done for 50 ps within the *NpT*-ensemble with a Berendsen thermostat and barostat⁴⁴ and damping constant $\tau_p = 2500$ fs. The box dimensions were set to the average of the last 25 ps of the *NpT*-equilibration.

Defect tracking was performed using a dynamic site-based analysis that follows the idea of the site-projection approach implemented in the site-analysis code.⁴⁶ For each defect species, the simulation supercell is partitioned into discrete, space-filling, non-overlapping volumes (sites), constructed separately for each MD frame from the instantaneous positions of the framework Pb atoms. Mobile Cs and I/Br atoms are then assigned to a specific site at each MD frame by projection onto these volumes.

To track all defects, we used a dynamic Voronoi decomposition of the simulation cell. At every MD frame, the midpoint of each pair (halides) or octet (Cs) of nearest-neighbor Pb atoms was computed from their instantaneous positions, with these midpoints used as seeds for a standard (per-frame) Voronoi decomposition. In the non-defective structure, every site is occupied by exactly one Cs or halide atom. Therefore, we associate unoccupied sites with vacancies, and doubly occupied sites with interstitials.

The mean squared displacement (MSD) has been calculated with the AMS MSD tool,⁴³ accord-

ing to

$$\text{MSD}(t) = \langle |r(t) - r(0)|^2 \rangle, \quad (1)$$

where $r(t)$ is the position of the defect at time t and $r(0)$ the initial position. The brackets indicate an average over all time origins with a time window of 5 ns. The diffusion coefficient D is obtained through a linear fit of the MSD according to

$$D = \frac{1}{2d} \frac{d}{dt} \text{MSD}(t), \quad (2)$$

where d is the dimensionality of the diffusion. For the determination of directional diffusion coefficients, we calculate the MSD separately for each Cartesian direction and set $d = 1$.

All atomic structures shown in this work, were generated using OVITO version 3.10.2.⁴⁷ Furthermore, we have used its implementation of polyhedral template matching⁴⁸ to determine the PbX_6 octahedrons.

3 Results and discussion

To systematically probe the influence of ordered halide layers on defect migration, we evaluated mass transport in $\text{od-CsPbBr}_2\text{I}$ and od-CsPbBrI_2 and compared it to that in randomly mixed $\text{ud-CsPbBr}_x\text{I}_{3-x}$, $x = 1$ or 2 , as well as to those in CsPbI_3 and CsPbBr_3 . Each system contains a single point defect, noted as V_S for a vacancy or I_S for an interstitial with $S = \text{I, Br, Cs}$. We are predominantly focusing on the atomistic migration behavior of the defect, using the Voronoi cell method to keep track of its migration path. Subsequently, we link this to the macroscopic diffusion behavior of the corresponding ionic species.

We first consider Cs vacancies and interstitials and elucidate the effect of anisotropic strain introduced by the layered halide structure on their motion. Next we focus on halide vacancies and interstitials, establishing the role played by the different bonding strengths of Pb-Br and Pb-I bonds. We do not look at Pb point defects, as these are immobile at the temperature and time range considered here.^{49,50}

3.1 Cesium defects and strain

Experimental and computational studies of defect motion in halide perovskites typically focus on halide defects. Although these are certainly important, A-site cation defects, Cs vacancies and interstitials in this case, are also mobile.^{51–53} First-principles studies show A-site defects should be prevalent, and compound defects further complicate the defect landscape, motivating explicit study of Cs migration.^{54,55} Despite A-site defects being electronically benign, A-site ions stabilize the perovskite lattice, so their migration may trigger structural phase changes.

Using the Voronoi-scheme we track the position over time of V_{Cs} and I_{Cs} . The results are given in Fig. 2 a). For V_{Cs} a jump to or across Pb-I layers is strongly suppressed, and motion takes place predominantly within the Pb-Br layers. Diffusion of I_{Cs} is even more anisotropic and strictly two-dimensional throughout the entire simulation.

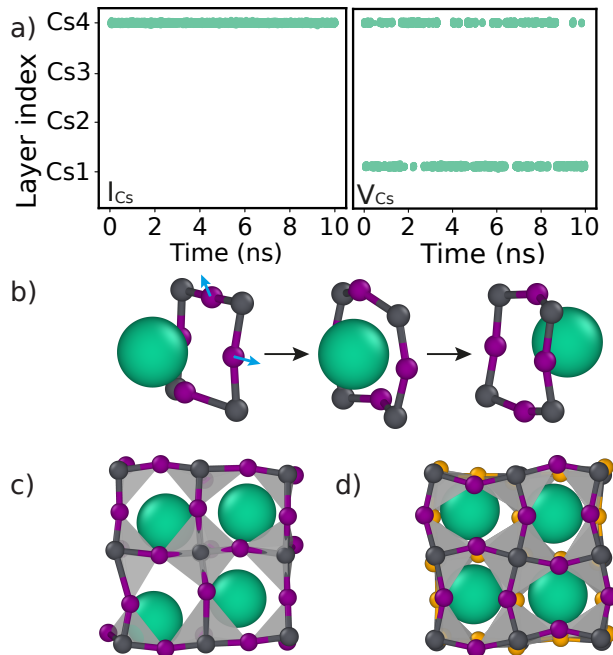


Figure 2: a) Positions of interstitial and vacancy, I_{Cs} , V_{Cs} , vs. simulation time in $\text{od-CsPbBr}_2\text{I}$ (for position labels, see Fig. 1); b) migration event with gate opening in $\alpha\text{-CsPbI}_3$; snapshots of c) $\alpha\text{-CsPbI}_3$ and d) $\text{od-CsPbBr}_2\text{I}$ structures.

The migration of Cs through the lattice is conceptually simple. For both interstitial and vacancy, a migration event consists of a Cs species crossing one of the sides of the cuboid formed by

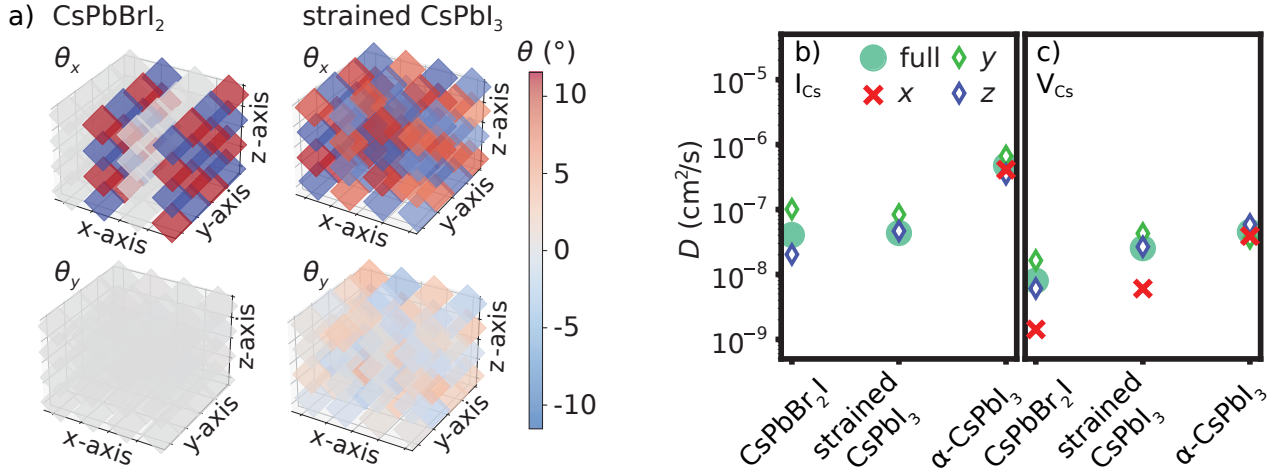


Figure 3: a) Time-averaged octahedral tilt angles with respect to x and y axes, θ_x and θ_y , in CsPbBr₂I and strained CsPbI₃ (full tilt analysis in SI Note 3.1); b), c) diffusion coefficients of Cs interstitial and vacancy, I_{Cs} , V_{Cs} , in CsPbBr₂I, strained CsPbI₃, and unstrained α -CsPbI₃. Diffusion of I_{Cs} in od-CsPbBr₂I and strained CsPbI₃ was too slow to gather enough data for the MSD analysis.

the eight PbX₆ octahedrons surrounding it. Such a crossing is accompanied by a gate-opening rearrangement of the surrounding octahedrons, as shown in Fig. 2 b). In α -CsPbBr₃ and α -CsPbI₃, these rearrangements take place along all three cartesian axes with equal probability at high temperatures. Layered MPHs show more structural rigidity in certain directions, as illustrated by comparing the octahedral tilts and window shapes of α -CsPbI₃ (Fig. 2 c) with those in CsPbBr₂I (Fig. 2 d).

We propose that the anisotropic diffusion of Cs defects is caused by the strain induced by linking the differently sized PbI₄X₂ and PbBr₄X₂ octahedra, which forces the PbI₄X₂ octahedra to tilt, as shown in Fig. 2 d). This locks Pb-I-Pb angles and suppresses the gate-opening motion required for a Cs atom to jump to the adjacent lattice site.

We monitor the octahedral tilting angles relative to the cartesian axes and calculate their time average θ_x , θ_y and θ_z along the MD trajectories. The octahedra in the Pb-I layers of the CsPbBr₂I lattice are tilted with respect to the normal to those layers, whereas in both other dimensions the octahedral tilt is negligible ($|\theta_x| \approx 12^\circ$, $\theta_y \approx 0$, $\theta_z \approx 0$). The tilts of neighboring octahedra have alternating signs, arranged in a checkerboard-like pattern, cf. Fig. 3 a). The octahedra in the Pb-Br layers have time-averaged tilting angles close to zero.

To isolate the effect of strain from chemical composition, we apply biaxial strain to pristine α -CsPbI₃ and α -CsPbBr₃ structures to replicate the octahedral tilt patterns observed in layered mixed-halide perovskites. In particular, we fix the lattice constant of α -CsPbI₃ in the x -direction, and apply compressive strain by reducing the lattice constants in the y - and z -directions. This results in a checkerboard octahedral tilting pattern with θ_x similar to that observed in CsPbBr₂I, see Fig. 3 a). There is some tilting in the y - and z -direction, but as $|\theta_y| \approx |\theta_z| = 2.1^\circ \ll |\theta_x| = 9.4^\circ$, this structure should be a reasonable representation of that of the Pb-I layers in CsPbBr₂I. In a similar way, tensile strain is applied to the α -CsPbBr₃ lattice to confirm that no octahedral tilting is introduced in Pb-Br layers. The exact procedure and tests can be found in the SI Note 3.2.

We have determined the diffusion coefficients at $T = 700\text{K}$ of Cs interstitials and vacancies in x -, y - and z -directions in strained and α -CsPbI₃ and compare them with those in CsPbBr₂I; the results are shown in Figures 3 b) and c). As one expects, α -CsPbI₃, which has a cubic structure, shows isotropic migration for Cs defects. In strained CsPbI₃, diffusion becomes anisotropic, and, what is more important, the directional diffusion coefficients become very similar to those in CsPbBr₂I.

Both V_{Cs} and I_{Cs} show a pronounced preference

for migration within the layers. In the case of Cs interstitials we even see a complete suppression of migration events in x -direction, as shown in Fig. 3 b). Tab. 1 gives the residence times of interstitials being oriented along the x -axis. We observe that this is only the case in a small time fraction of the simulation, which limits the overall attempt rate of a jump in the x -direction. In other words, one expects Cs interstitials to be confined perpendicular to x in yz layers. V_{Cs} is confined less strongly, but still the diffusion coefficients in y -, and z -directions are an order of magnitude larger than that in the x -direction, Fig. 3 c).

Table 1: The fraction of time I_{Cs} is oriented along the x -axis and perpendicular to it during the simulation. Without structural bias, we expect: $\perp x : \parallel x = 2 : 1$.

Config	$\perp x$ (%)	$\parallel x$ (%)
α -CsPbI ₃	66.7	33.3
od-CsPbBr ₂ I	98.0	2.0
strained CsPbI ₃	93.4	6.6

To add an explanation of the diffusion anisotropy on the basis of structures, the chessboard-like tilting pattern of the PbX_6 octahedra, with $|\theta_x| \neq 0$ and $|\theta_y| \approx 0$, $|\theta_z| \approx 0$, locks certain Pb-I-Pb angles in the yz -plane (Fig. 2 d)). This suppresses the gate-opening motion required for a Cs atom to jump to the adjacent lattice site along the x -direction (Fig. 1).

We have furthermore studied the influence of tensile strain along the y - and z -axes of the α -CsPbBr₃ lattice. Here, a slight reduction of octahedral tilts was accompanied by an approximately two times higher diffusion coefficients in the x -direction compared to y and z . Concrete values can be found in the SI Tab. S1 in Note 1 and Fig. S6 in Note 3.2.

3.2 Halide defects and chemical composition

Halide defects have been widely studied in MHPs, as they are relatively easily formed and are quite mobile, and thus thought to strongly influence ionic conductivity and structural and chemical stability.^{35,39,40,54,55} Similar to the Cs defects, we ob-

serve confinement to layers for both vacancies and interstitials. However, the underlying reasons differ somewhat, as it turns out that strain is not the only factor guiding the diffusion of halide point defects, but the chemical distinction between Br and I plays a distinct role.

To isolate the role of halide composition from directional strain effects, we compare diffusion in od-CsPbBr₂I and od-CsPbBrI₂ structures with ud-CsPbBr₂I and ud-CsPbBrI₂. We only present the results for a removed and added Br here, as the results for I defects are qualitatively similar. Results for the latter can be found in the SI Note 2.

The basic reason for these similarities is that both migration of interstitial and vacancy typically proceed through kick-out processes where the initial defect interchanges role with a lattice halide. So ultimately it is the structure and composition of the lattice that determines the migration, not the species of the initial defect.

3.2.1 Halide interstitials

As a first step we focus on the anisotropy of diffusion of the halide interstitial. As shown in Fig. 4 a) and b), we see that the interstitial in both od-CsPbBr₂I and od-CsPbBrI₂ is largely confined to the majority layers, i.e., Br layers and I layers respectively. As these majority layers are subject to opposite strain, i.e. tensile on the Br layer and compressive on the I layer, strain cannot be the governing factor here.

We track the identity of the interstitial over time in Tab. 2. In CsPbBr₂I, the interstitial is a Br atom most of the time, whereas in CsPbBrI₂ it is an I atom. Note that as the halide interstitial mainly migrates via a kick-out mechanism, it can easily change character over time, i.e., a Br (I) interstitial can kick out a lattice I (Br), where the latter then becomes the interstitial. We thus observe that in the interstitial adopts the character of the majority halide, i.e., Br in CsPbBr₂I and I in CsPbBrI₂.

We argue that this adoption is associated with the preferred bonding configurations of the interstitial. The most favored position of a halide interstitial is a bridge site between two neighboring Pb sites, where in fact it then forms a double bridge together with the lattice halide that is al-

Table 2: The elementally resolved diffusion coefficients D_X , the time fraction of the interstitial bridge type and of the layer type population along the x -axis during the simulation.

Structure	D_X ($\times 10^{-8}$ cm 2 s $^{-1}$)		Interstitial type			Layer type population		
	$X = \text{Br}$	$X = \text{I}$	$p_{2\text{I}}$ (%)	p_{BrI} (%)	$p_{2\text{Br}}$ (%)	p_{Pb} (%)	p_{Cs} (%)	$p_{\text{Pb}}/p_{\text{Cs}}$
α -CsPbBr $_3$	24.4	-	-	-	100	67.49	32.51	2
α -CsPbI $_3$	-	29.7	100	-	-	66.44	33.56	2
od-CsPbBr $_2$ I	10.2	0.3	0	0.02	99.98	93.65	6.35	14.7
ud-CsPbBr $_2$ I	10.7	0.1	0	0.12	99.87	68.13	31.87	2.1
od-CsPbBrI $_2$	0.2	6.0	99.33	0.67	0	92.28	7.72	12
ud-CsPbBrI $_2$	0.4	12.5	90.25	9.64	0.1	79.4	20.6	3.9

ready there.⁴⁰ The halide interstitial preferentially forms a double bridge with a halide of the same kind, i.e., Br with Br and I with I, see Tab. 2. This observation does not depend on whether the Br and I in the CsPbBr $_2$ I and CsPbBrI $_2$ materials are ordered in layers, or the materials are random alloys. It follows that the preference is dictated by the local chemical bonding.

This analysis is corroborated by an inspection of the interstitial position with respect to the metal cations over time, see Tab. 2. One can interpret the perovskite structure as a (100) stacking PbX $_2$ and CsX layers. If the interstitial would have no preference while migrating, we would see a $p_{\text{Pb}}/p_{\text{Cs}}$ ratio of two. However, we find significantly larger values in CsPbBr $_2$ I of 14.7 and in CsPbBrI $_2$ of 12.0, which indicate that the migration is dictated by the chemical bonding pattern.

The favored bridge positions of interstitials bring about distinct diffusion paths. Fig. 4 c) shows the interstitial Br in od-CsPbBr $_2$ I in a characteristic Pb-Br $_2$ -Pb bridge position together with a lattice Br. Hopping to neighboring site involves only a short distance and can take place unhindered in all possible directions. Migration within the Br layers then proceeds as a sequence of such nearest neighbor hopping events.

This mechanism is suppressed in the I layers within od-CsPbBr $_2$ I, where the strain on the iodine layer also affects the interstitial geometry as shown in Fig. 4 d). The Pb-I $_2$ -Pb bridge is no longer free to rotate in all space directions equally, but has a preference for the two I to be stacked in the x -direction. This hinders jumps of the interstitial in the y -direction.

Tab. 2 lists the extracted diffusion coefficients for interstitial diffusion. In general, mixing halides

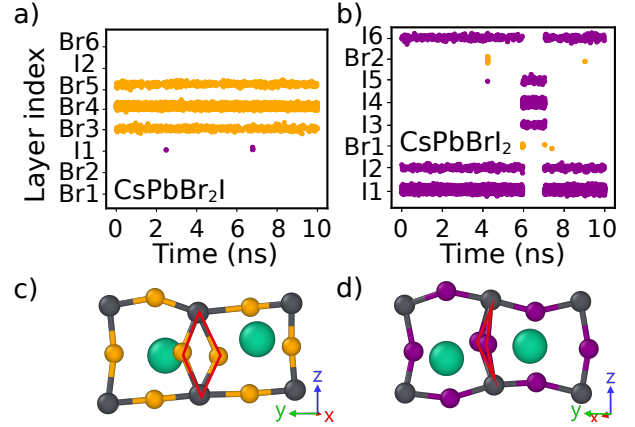


Figure 4: Position vs. simulation time of interstitial I_x in a) od-CsPbBr $_2$ I and b) od-CsPbBrI $_2$ (for position labels, see Fig. 1); yellow, purple indicate Br, I interstitials, respectively. Snap shots of c) Pb-Br $_2$ -Pb and d) Pb-I $_2$ -Pb double bridge interstitial geometries in od-CsPbBr $_2$ I.

reduces the interstitial mobility. In all structures, the overall diffusion coefficient is reduced by more than 50%. The lowest value is observed in od-CsPbBrI $_2$, where the interstitial is mostly migrating in the Pb-I layers. Here, the favored bridge position, as shown in Fig. 4 d) suppresses migration within the Pb-I layer, as discussed above.

In ordered and unordered structures in CsPbBr $_2$ I and in CsPbBrI $_2$, the elementally resolved diffusion coefficients are very similar. Thus in conclusion, the dominant steering feature for diffusion of halide interstitials in mixed halide perovskites is the halide composition.

3.2.2 Halide Vacancies

Fig. 5 shows the location of the vacancy in the od-CsPbBr $_2$ I and od-CsPbBrI $_2$ lattices dur-

ing the simulation. It is clear that the vacancy has a strong preference for migrating in the iodine layers. In CsPbBr_2I the migration is two-dimensional in a single Pb-I layer, whereas in CsPbBrI_2 it is somewhat more spread out but still very anisotropic. In the latter, the Pb-I layers are more populated than the Cs-I layers.

The migration pattern is consistent with the favored position of the vacancy on the basis of its energy landscape. Tab. 3 shows the total energies calculated for the vacancy at different positions in the CsPbBr_2I and CsPbBrI_2 lattices (with details in SI Note 2.1). It clearly demonstrates that the energies for vacancies in Br layers are higher than in I layers. Furthermore, the vacancy prefers the Pb-I layers over Cs-I layers, which is consistent with the observation that the vacancy migrates predominantly in the Pb-I layers, and not in the Cs-I layers.

These findings are in line with observations of vacancy diffusion in simple atomic lattices, where compressive strain enhances diffusion of vacancies, and tensile strain hinders it.⁴² The rationale behind this is that compressive (tensile) strain stabilizes (destabilizes) the vacancy, and decreases (increases) the diffusion barrier. As discussed above, in layered $\text{CsPbBr}_x\text{I}_{3-x}$ compounds the I layers are under compressive stress, whereas the Br layers are under tensile stress.

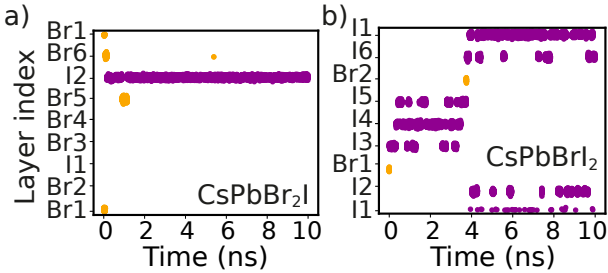


Figure 5: Position of vacancy V_X vs. simulation time in in a) $\text{od-CsPbBr}_2\text{I}$ and b) od-CsPbBrI_2 (for position labels, see Fig. 1); yellow, purple indicate positions in Br and I layers, respectively.

Tab. 4 shows the elementally resolved diffusion coefficients for a halide vacancy in CsPbBr_2I and CsPbBrI_2 in the ordered, as well as in the random structures, compared to $\alpha\text{-CsPbBr}_3$ and $\alpha\text{-CsPbI}_3$. The results clearly show that vacancy-mediated mass transport in mixed-halide phases

Table 3: Total energies and standard error of the mean in CsPbBr_2I and CsPbBrI_2 with a halide vacancy.

CsPbBr_2I		CsPbBrI_2	
Position	ΔE_{tot} (eV)	Position	ΔE_{tot} (eV)
Cs-Br	0.18 ± 0.03	Cs-I	0.04 ± 0.02
Pb-Br	0.16 ± 0.03	Pb-Br	0.18 ± 0.02
Pb-I	0 ± 0.03	Pb-I	0 ± 0.02

is predominantly iodine migration. This holds for the ordered as well as the unordered structures. However, the difference between the diffusion coefficients of iodine and bromine migration in ordered structures is one to two orders of magnitude, whereas in unordered structures it is only a factor of 1.2-3.6.

In ordered structures, the layered arrangement combined with the preference of the vacancy for Pb-I sites strongly favors iodine migration over bromine migration. In unordered structures, asymmetric local environments enable both halides to participate in vacancy diffusion, though iodine remains dominant.

Table 4: Elementally resolved diffusion coefficients D_X for a halide vacancy in $\text{CsPbBr}_x\text{I}_{3-x}$. In all systems a single bromine has been removed, except for the pristine $\alpha\text{-CsPbI}_3$, where a single iodine has been removed.

Structure	D_X ($\times 10^{-9} \text{ cm}^2 \text{ s}^{-1}$)	
	$X = \text{Br}$	$X = \text{I}$
$\alpha\text{-CsPbBr}_3$	3.9	-
$\alpha\text{-CsPbI}_3$	-	9.7
$\text{od-CsPbBr}_2\text{I}$	0.0	23.8
$\text{ud-CsPbBr}_2\text{I}$	2.3	8.3
od-CsPbBrI_2	0.9	13.6
ud-CsPbBrI_2	6.3	7.4

We observe a faster diffusion in ordered structures, compared to the pristine and unordered structures. In addition, we see a trend in the mixed structures where a higher Br content leads to an increase in iodine diffusion coefficient. This is again consistent with the strain argument mentioned above. Compressive strain promotes iodine diffusion. In unordered structures with a higher Br content the compressive strain on the I distributed

in the lattice is largest among the systems we have considered here.

4 Summary and conclusions

In this work, we have studied the defect migration in mixed-halide perovskites $\text{CsPbBr}_x\text{I}_{3-x}$ with different halide ordering by means of molecular dynamics simulations using a reactive force field (ReaxFF). In particular, we investigated atomically layered Br and I structures similar to the ones realized experimentally.³⁰

With the help of a dynamic Voronoi analysis,^{56,57} we have characterized the defect migration. We have found that in CsPbBr_2I and CsPbBrI_2 defect migration is very anisotropic. For Cs and halide interstitials and vacancies the rate of defect migration parallel to the layers is comparable to that observed in single-halide or random mixed-halide perovskites. However, defect migration perpendicular to ordered Br and I layers is markedly slower.

We have established the factors governing the anisotropic migration in these perovskites. For Cs vacancies and interstitials the anisotropy is fully determined by the anisotropic strain introduced by ordering halides in layers in $\text{CsPbBr}_x\text{I}_{3-x}$. The compressive strain introduced in the latter freezes a tilting pattern in the PbX_6 octahedra, severely hindering Cs diffusion. At the same time, this compressive strain stabilizes the halide vacancies within the Pb-I layers, so the latter have a strong tendency to migrate within those.

While influenced by strain, migration of halide interstitials is also governed by chemical bonding. In its most stable configuration, a halide interstitial forms a double bridge between two Pb sites with another (a lattice) halide. The system has a strong preference for a double bridge pair of the same halide, Pb-II-Pb or Pb-BrBr-Pb. Diffusion is then governed by forming such pairs along the migration path, which results in a strong anisotropy in layered perovskites. Applying a rare event sampling approach may further clarify the local initialization conditions governing defect migration.^{58,59}

In short, we have established that strain engineering, here done through halide layering, can confine defect motion to specific crystallographic

planes. In a device under operating conditions, ionic motion can be influenced by electric fields, which may have unwanted consequences such as hysteresis in IV curves, or even enhanced degradation at the perovskite surfaces and interfaces. In layered perovskites such motion can be suppressed by having the layers perpendicular to the electric field. In general, the current work encourages further effort towards strain engineering in perovskite solar cells.

Acknowledgement S.T. and K.W. acknowledge funding from Vidi (project no. VI.Vidi.213.091) from the Dutch Research Council (NWO). This work used the Dutch national e-infrastructure with the support of the SURF Cooperative using grant no. EINF-11274. We thank Benjamin J. Morgan for helpful discussions regarding tracking mobile defects using site-projection methods. We thank Viren Tyagi for fruitful exchanges on molecular simulations of defects.

Supporting Information Available

Additional migration data on cesium and halide defects; procedure for obtaining energy landscapes; detailed tilt analysis of strained and layered systems as well as the procedure of application of biaxial strain.

References

- (1) Filip, M. R.; Eperon, G. E.; Snaith, H. J.; Giustino, F. Steric Engineering of Metal-Halide Perovskites with Tunable Optical Band Gaps. *Nat. Commun.* **2014**, *5*, 5757.
- (2) Unger, E. L.; Kegelmann, L.; Suchan, K.; Sörell, D.; Korte, L.; Albrecht, S. Roadmap and Roadblocks for the Band Gap Tunability of Metal Halide Perovskites. *J. Mater. Chem. A* **2017**, *5*, 11401–11409.
- (3) Niebur, A.; Klein, E.; Lesyuk, R.; Klinke, C.; Lauth, J. Understanding the Optoelectronic Processes in Colloidal 2D Multi-Layered MAPbBr₃ Perovskite Nanosheets: Funneling, Recombination and Self-Trapped Excitons. *Adv. Opt. Mater.* **2025**, *13*, 2402923.
- (4) Le Corre, V. M.; Duijnste, E. A.; El Tambouli, O.; Ball, J. M.; Snaith, H. J.; Lim, J.; Koster, L. J. A. Revealing Charge Carrier Mobility and Defect Densities in Metal Halide Perovskites via Space-Charge-Limited Current Measurements. *ACS Energy Lett.* **2021**, *6*, 1087–1094.
- (5) Herz, L. M. Charge-Carrier Mobilities in Metal Halide Perovskites: Fundamental Mechanisms and Limits. *ACS Energy Lett.* **2017**, *2*, 1539–1548.
- (6) Kumar Tailor, N.; Yukta; Ranjan, R.; Ranjan, S.; Sharma, T.; Singh, A.; Garg, A.; Singh Nalwa, K.; Kumar Gupta, R.; Satapathi, S. The Effect of Dimensionality on the Charge Carrier Mobility of Halide Perovskites. *J. Mater. Chem. A* **2021**, *9*, 21551–21575.
- (7) Snaith, H. J. Perovskites: The Emergence of a New Era for Low-Cost, High-Efficiency Solar Cells. *J. Phys. Chem. Lett.* **2013**, *4*, 3623–3630.
- (8) Zhang, W.; Eperon, G. E.; Snaith, H. J. Metal Halide Perovskites for Energy Applications. *Nat. Energy* **2016**, *1*, 16048.
- (9) Soto-Montero, T.; Morales-Masis, M. Laser Deposition of Metal Halide Perovskites. *ACS Energy Lett.* **2024**, *9*, 4199–4208.
- (10) Green, M. A.; Dunlop, E. D.; Yoshita, M.; Kopidakis, N.; Bothe, K.; Siefert, G.; Hao, X.; Jiang, J. Y. Solar Cell Efficiency Tables (Version 66). *Prog. Photovolt. Res. Appl.* **2025**, *33*, 795–810.
- (11) Best Research-Cell Efficiency Chart | Photovoltaic Research | NREL. <https://www.nrel.gov/pv/cell-efficiency>.
- (12) Xiang, W.; Liu, S. F.; Tress, W. A Review on the Stability of Inorganic Metal Halide Perovskites: Challenges and Opportunities for Stable Solar Cells. *Energy Environ. Sci.* **2021**, *14*, 2090–2113.
- (13) Jiang, J.; Liu, F.; Tranca, I.; Shen, Q.; Tao, S. Atomistic and Electronic Origin of Phase Instability of Metal Halide Perovskites. *ACS Appl. Energy Mater.* **2020**, *3*, 11548–11558.
- (14) Leijtens, T.; Eperon, G. E.; Noel, N. K.; Habisreutinger, S. N.; Petrozza, A.; Snaith, H. J. Stability of Metal Halide Perovskite Solar Cells. *Adv. Energy Mater.* **2015**, *5*, 1500963.
- (15) Chen, Z.; Brocks, G.; Tao, S.; Bobbert, P. A. Unified Theory for Light-Induced Halide Segregation in Mixed Halide Perovskites. *Nat. Commun.* **2021**, *12*, 2687.
- (16) Steele, J. A.; Lai, M.; Zhang, Y.; Lin, Z.; Hofkens, J.; Roeffaers, M. B. J.; Yang, P. Phase Transitions and Anion Exchange in All-Inorganic Halide Perovskites. *Acc. Mater. Res.* **2020**, *1*, 3–15.
- (17) Chang, X.; Li, W.; Zhu, L.; Liu, H.; Geng, H.; Xiang, S.; Liu, J.; Chen, H. Carbon-Based CsPbBr₃ Perovskite Solar Cells: All-Ambient Processes and High Thermal Stability. *ACS Appl. Mater. Interfaces* **2016**, *8*, 33649–33655.
- (18) Yao, Z.; Zhao, W.; Liu, S. F. Stability of the CsPbI₃ Perovskite: From Fundamentals to

- Improvements. *J. Mater. Chem. A* **2021**, *9*, 11124–11144.
- (19) Eperon, G. E.; Stranks, S. D.; Menelaou, C.; Johnston, M. B.; Herz, L. M.; Snaith, H. J. Formamidinium Lead Trihalide: A Broadly Tunable Perovskite for Efficient Planar Heterojunction Solar Cells. *Energy Environ. Sci.* **2014**, *7*, 982–988.
- (20) Shockley, W.; Queisser, H. J. Detailed Balance Limit of Efficiency of P-n Junction Solar Cells. *J. Appl. Phys.* **1961**, *32*, 510–519.
- (21) Jin, B.; Yang, D.; Gong, R.; Sugai, Y.; Lan, D.; Steele, J. A.; Zhang, X. Strain Analysis of Black-to-Yellow Phase Transitions in CsPbI₃. *InfoMat* **2026**, *8*, e70084.
- (22) Stoumpos, C. C.; Kanatzidis, M. G. The Renaissance of Halide Perovskites and Their Evolution as Emerging Semiconductors. *Acc. Chem. Res.* **2015**, *48*, 2791–2802.
- (23) Marronnier, A.; Roma, G.; Boyer-Richard, S.; Pedesseau, L.; Jancu, J.-M.; Bonnassieux, Y.; Katan, C.; Stoumpos, C. C.; Kanatzidis, M. G.; Even, J. Anharmonicity and Disorder in the Black Phases of Cesium Lead Iodide Used for Stable Inorganic Perovskite Solar Cells. *ACS Nano* **2018**, *12*, 3477–3486.
- (24) Straus, D. B.; Guo, S.; Abeykoon, A. M.; Cava, R. J. Understanding the Instability of the Halide Perovskite CsPbI₃ through Temperature-Dependent Structural Analysis. *Adv. Mater.* **2020**, *32*, 2001069.
- (25) Steele, J. A. et al. An Embedded Interfacial Network Stabilizes Inorganic CsPbI₃ Perovskite Thin Films. *Nat. Commun.* **2022**, *13*, 7513.
- (26) Goldschmidt, V. M. Die Gesetze der Kristallochemie. *Naturwissenschaften* **1926**, *14*, 477–485.
- (27) Näsström, H.; Becker, P.; Márquez, J. A.; Shargaieva, O.; Mainz, R.; Unger, E.; Unold, T. Dependence of Phase Transitions on Halide Ratio in Inorganic CsPb(Br_xI_{1-x})₃ Perovskite Thin Films Obtained from High-Throughput Experimentation. *J. Mater. Chem. A* **2020**, *8*, 22626–22631.
- (28) Mannino, G.; Deretzis, I.; Smecca, E.; La Magna, A.; Alberti, A.; Ceratti, D.; Cahen, D. Temperature-Dependent Optical Band Gap in CsPbBr₃, MAPbBr₃, and FAPbBr₃ Single Crystals. *J Phys Chem Lett* **2020**, *11*, 2490–2496.
- (29) Li, X.; Tan, Y.; Lai, H.; Li, S.; Chen, Y.; Li, S.; Xu, P.; Yang, J. All-Inorganic CsPbBr₃ Perovskite Solar Cells with 10.45% Efficiency by Evaporation-Assisted Deposition and Setting Intermediate Energy Levels. *ACS Appl. Mater. Interfaces* **2019**, *11*, 29746–29752.
- (30) Deng, J.; Yuan, S.; Xiong, H.; Ma, Z.; Wu, W.; Wang, M.; Lou, Z.; Fan, J.; Li, W. Br-I Ordered CsPbBr₂I Perovskite Single Crystal toward Extremely High Mobility. *Chem* **2023**, *9*, 1929–1944.
- (31) Teunissen, J. L.; Braeckvelt, T.; Skvortsova, I.; Guo, J.; Pradhan, B.; Debroye, E.; Roeffaers, M. B. J.; Hofkens, J.; Van Aert, S.; Bals, S.; Rogge, S. M. J.; Van Speybroeck, V. Additivity of Atomic Strain Fields as a Tool to Strain-Engineering Phase-Stabilized CsPbI₃ Perovskites. *J. Phys. Chem. C* **2023**, *127*, 23400–23411.
- (32) Steele, J. A.; Solano, E.; Jin, H.; Prakasam, V.; Braeckvelt, T.; Yuan, H.; Lin, Z.; de Kloe, R.; Wang, Q.; Rogge, S. M. J.; Van Speybroeck, V.; Chernyshov, D.; Hofkens, J.; Roeffaers, M. B. J. Texture Formation in Polycrystalline Thin Films of All-Inorganic Lead Halide Perovskite. *Adv. Mater.* **2021**, *33*, 2007224.
- (33) Lin, Y.; Li, J.; Zheng, J.; Shao, J.; Wu, M.; Liu, Y.; Wu, Z.; Fan, J.; Li, W. I-Br Ordered DMAPbI_{3-x}Br_x Crystal Intermediates Enabling High-Quality CsPbI_{3-x}Br_x Inorganic Perovskite Thin Films in Solar Cells. *ACS Appl. Mater. Interfaces* **2026**, *18*, 1501–1511.

- (34) Steele, J. A. et al. Thermal Unequilibrium of Strained Black CsPbI₃ Thin Films. *Science* **2019**, *365*, 679–684.
- (35) Pols, M.; Vicent-Luna, J. M.; Filot, I.; van Duin, A. C. T.; Tao, S. Atomistic Insights Into the Degradation of Inorganic Halide Perovskite CsPbI₃: A Reactive Force Field Molecular Dynamics Study. *J. Phys. Chem. Lett.* **2021**, *12*, 5519–5525.
- (36) Delugas, P.; Caddeo, C.; Filippetti, A.; Mattoni, A. Thermally Activated Point Defect Diffusion in Methylammonium Lead Trihalide: Anisotropic and Ultrahigh Mobility of Iodine. *J. Phys. Chem. Lett.* **2016**, *7*, 2356–2361.
- (37) Mattoni, A.; Argiolas, S.; Cozzolino, G.; Dell'Angelo, D.; Filippetti, A.; Caddeo, C. Many-Body MYP2 Force-Field: Toward the Crystal Growth Modeling of Hybrid Perovskites. *J. Chem. Theory Comput.* **2024**, *20*, 6781–6789.
- (38) Phung, N.; Al-Ashouri, A.; Meloni, S.; Mattoni, A.; Albrecht, S.; Unger, E. L.; Merdasa, A.; Abate, A. The Role of Grain Boundaries on Ionic Defect Migration in Metal Halide Perovskites. *Adv. Energy Mater.* **2020**, *10*, 1903735.
- (39) Pols, M.; Brouwers, V.; Calero, S.; Tao, S. How Fast Do Defects Migrate in Halide Perovskites: Insights from on-the-Fly Machine-Learned Force Fields. *Chem. Commun.* **2023**, *59*, 4660–4663.
- (40) Tyagi, V.; Pols, M.; Brocks, G.; Tao, S. Tracing Ion Migration in Halide Perovskites with Machine Learned Force Fields. *J. Phys. Chem. Lett.* **2025**, *16*, 5153–5159.
- (41) Pols, M.; van Duin, A. C. T.; Calero, S.; Tao, S. Mixing I and Br in Inorganic Perovskites: Atomistic Insights from Reactive Molecular Dynamics Simulations. *J. Phys. Chem. C* **2024**, *128*, 4111–4118.
- (42) Tyagi, V.; Pols, M.; Brocks, G.; Tao, S. Halide Diffusion in Mixed-Halide Perovskites and Heterojunctions. *Chem. Mater.* **2026**,
- (43) Rüger, R.; Franchini, M.; Trnka, T.; Yakovlev, A.; van Lenthe, E.; Philipsen, P.; van Vuren, T.; Klumpers, B.; Soini, T. Ams 2024.1. SCM, Theoretical Chemistry, Vrije Universiteit, Amsterdam, The Netherlands, 2024.
- (44) Berendsen, H. J. C.; Postma, J. P. M.; van Gunsteren, W. F.; DiNola, A.; Haak, J. R. Molecular Dynamics with Coupling to an External Bath. *J. Chem. Phys.* **1984**, *81*, 3684–3690.
- (45) Martyna, G. J.; Klein, M. L.; Tuckerman, M. Nosé–Hoover Chains: The Canonical Ensemble via Continuous Dynamics. *J. Chem. Phys.* **1992**, *97*, 2635–2643.
- (46) Morgan, B. J. Site-Analysis: Python Module for Analysing Molecular Dynamics Simulations of Ion Transport. 2026.
- (47) Stukowski, A. Visualization and Analysis of Atomistic Simulation Data with OVITO—the Open Visualization Tool. *Modell. Simul. Mater. Sci. Eng.* **2009**, *18*, 015012.
- (48) Larsen, P. M.; Schmidt, S.; Schiøtz, J. Robust structural identification via polyhedral template matching. *Model. Simul. Mater. Sci. Eng.* **2016**, *24*, 055007.
- (49) Eames, C.; Frost, J. M.; Barnes, P. R. F.; O'Regan, B. C.; Walsh, A.; Islam, M. S. Ionic Transport in Hybrid Lead Iodide Perovskite Solar Cells. *Nat. Commun.* **2015**, *6*, 7497.
- (50) Eperon, G. E.; Ginger, D. S. B-Site Metal Cation Exchange in Halide Perovskites. *ACS Energy Lett.* **2017**, *2*, 1190–1196.
- (51) Eperon, G. E.; Beck, C. E.; Snaith, H. J. Cation Exchange for Thin Film Lead Iodide Perovskite Interconversion. *Mater. Horiz.* **2015**, *3*, 63–71.
- (52) Niemann, R. G.; Gouda, L.; Hu, J.; Tirosh, S.; Gottesman, R.; Cameron, P. J.; Zaban, A. Cs⁺ Incorporation into CH₃NH₃PbI₃ Perovskite: Substitution Limit and Stability Enhancement. *J. Mater. Chem. A* **2016**, *4*, 17819–17827.

- (53) Hu, Y.; Schlipf, J.; Wussler, M.; Petrus, M. L.; Jaegermann, W.; Bein, T.; Müller-Buschbaum, P.; Docampo, P. Hybrid Perovskite/Perovskite Heterojunction Solar Cells. *ACS Nano* **2016**, *10*, 5999–6007.
- (54) Xue, H.; Brocks, G.; Tao, S. Intrinsic Defects in Primary Halide Perovskites: A First-Principles Study of the Thermodynamic Trends. *Phys. Rev. Materials* **2022**, *6*, 055402.
- (55) Xue, H.; Vicent-Luna, J. M.; Tao, S.; Brocks, G. Compound Defects in Halide Perovskites: A First-Principles Study of CsPbI₃. *J. Phys. Chem. C* **2023**, *127*, 1189–1197.
- (56) Goldmann, B. A.; Rosenbach, C.; Evans, H. A.; Helm, B.; Wankmiller, B.; Maus, O.; Suard, E.; Nazar, L. F.; Hansen, M. R.; Morgan, B. J.; Islam, M. S.; Zeier, W. G. Rotational Stacking Faults in the Ionic Conductor Li₃ScCl₆. *Chem. Mater.* **2025**,
- (57) Krenzer, G.; Klarbring, J.; Tolborg, K.; Rossignol, H.; McCluskey, A. R.; Morgan, B. J.; Walsh, A. Nature of the Superionic Phase Transition of Lithium Nitride from Machine Learning Force Fields. *Chem. Mater.* **2023**, *35*, 6133–6140.
- (58) Wilke, K.; Tao, S.; Calero, S.; Lervik, A.; van Erp, T. S. NaCl Dissociation Explored Through Predictive Power Path Sampling Analysis. *J. Chem. Theory Comput.* **2025**, *21*, 4604–4614.
- (59) Roet, S.; Daub, C. D.; Riccardi, E. Chemistrees: Data-Driven Identification of Reaction Pathways via Machine Learning. *J. Chem. Theory Comput.* **2021**, *17*, 6193–6202.

Supplementary Information:
Anisotropic Defect Diffusion in Layered
CsPbBr_xI_{3-x} Perovskites

Konrad Wilke,[†] Mike Pols,[†] Titus S. van Erp,[‡] Geert Brocks,[¶] and Shuxia Tao^{*,†}

[†]*Department of Applied Physics and Science Education, Eindhoven University of Technology,
5600 MB, Eindhoven, The Netherlands*

[‡]*Department of Chemistry and Biomedical Science, Norwegian University of Science and
Technology, 7941 Trondheim, Norway*

[¶]*Department of Applied Physics and Science Education, Eindhoven University of Technology,
5600 MB, Eindhoven, The Netherlands; Computational Chemical Physics, Faculty of Science and
Technology and MESA+ Institute for Nanotechnology, University of Twente, Enschede 7500 AE,
The Netherlands.*

E-mail: s.x.tao@tue.nl

Contents

1	SI Note: Cs defects	S3
2	SI Note: Halide defects	S4
2.1	Halide vacancy energy landscapes	S7
3	SI Note: Influence of strain	S8
3.1	Layered Structures	S8
3.2	Applied biaxial strain to pristine α -CsPbBr ₃ and α -CsPbI ₃	S9
	References	S13

1 SI Note: Cs defects

This section provides additional data for Cs vacancy and interstitial diffusion, complementing the results presented in Section 3.1 of the main text. The Br and I layers in od-CsPbBr_xI_{3-x} structures are parallel to the yz-plane. In Fig. S1 we show the jumping of Cs along the x-axis, in Tab. S1 its the respective directional diffusion. Furthermore, we present the complementary values for directional orientation of I_{Cs} in further compounds in Tab. S2.

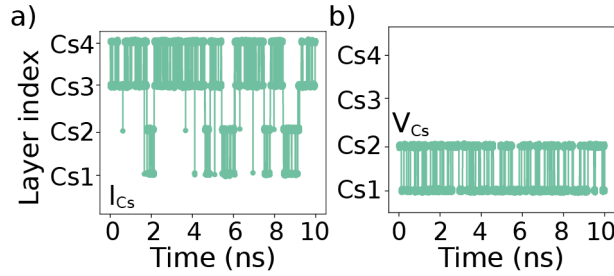


Figure S1: Layer index of a) the interstitial I_{Cs} and b) the vacancy V_{Cs} vs. simulation time in od-CsPbBrI₂. For the layer indices, see Fig. 1 in the main text.

Table S1: Elementally resolved total diffusion coefficients D_x and along the cartesian axes x , y , and z in $\times 10^8 \text{ cm}^2 \text{ s}^{-1}$ for systems with a vacancy V_{Cs} or an interstitial I_{Cs} at 700 K.

in $\times 10^8 \text{ cm}^2/\text{s}^{-1}$	V _{Cs}				I _{Cs}			
	D_{tot}	D_x	D_y	D_z	D_{tot}	D_x	D_y	D_z
α -CsPbBr ₃	1.2	2.0	1.2	0.7	70.1	97.5	62.3	50.4
strained CsPbBr ₃	0.9	1.5	0.3	0.9	61.7	101.0	31.0	50.6
od-CsPbBrI ₂	2.2	1.9	2.3	3.1	26.1	13.9	33.9	30.9

Table S2: The fraction of time that I_{Cs} is oriented along the x -axis and perpendicular to it.

Config	$\perp x$ (%)	$\parallel x$ (%)
ud-CsPbBrI ₂	31.2	68.8
od-CsPbBrI ₂	35.5	64.5
ud-CsPbBr ₂ I	32.5	67.5
α -CsPbBr ₃	32.3	67.7
strained CsPbBr ₃	42.6	57.4

2 SI Note: Halide defects

This section provides additional trajectory data and diffusion coefficients for halide vacancies and interstitials with an iodine defect, complementing the bromine-defect results presented in Section 3.2 of the main text. In Fig. S2 and Fig. S3 we present the layer index of the position of the defect, within $\text{od-CsPbBr}_2\text{I}$ and od-CsPbBrI_2 with a single iodine added or missing. The identity of the interstitial is presented in Tab. S3, complementary to Tab. 2 in the main text. Directional diffusion for all compounds with halide interstitials are presented in Tab. S4 and vacancies in Tab. S5.

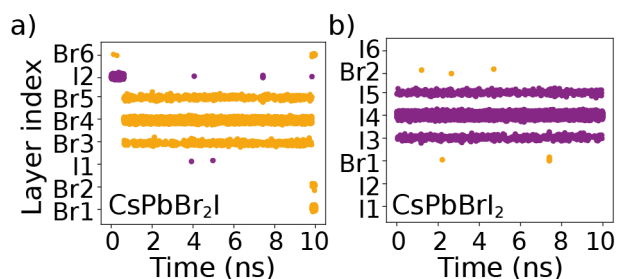


Figure S2: Layer index of I_x vs. simulation time in yellow when in Br layer, purple when in I layer, in a) $\text{od-CsPbBr}_2\text{I}$ and b) od-CsPbBrI_2 , starting with a single additional iodine interstitial. For the layer indices, see Fig. 1 in the main text.

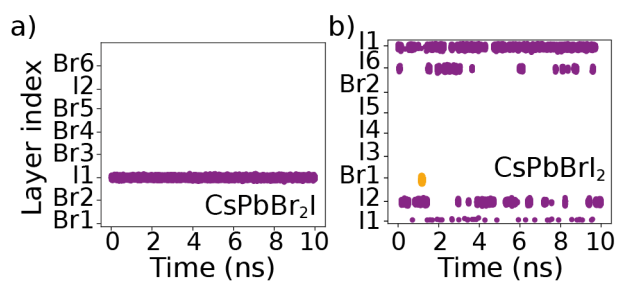


Figure S3: Layer index of V_x vs. simulation time in yellow when in Br layer, purple when in I layer in a) $\text{od-CsPbBr}_2\text{I}$ and b) od-CsPbBrI_2 , starting with a single iodine vacancy. For the layer indices, see Fig. 1 in the main text.

Table S3: Percentage of time an interstitial is part of a bridge configuration with two I (p_{2I}), one Br and one I (p_{BrI}) and two Br (p_{2Br}) in $\text{CsPbBr}_x\text{I}_{3-x}$, starting from a single added iodine. The interstitial type is identified as the center of a doubly occupied Voronoi cell.

Config	p_{2I} (%)	p_{BrI} (%)	p_{2Br} (%)
CsPbBrI₂			
ud-	97.1	2.9	0
od-	99.95	0.5	0
CsPbBr₂I			
ud-	0	0.03	99.97
od-	6.17	0.41	93.42

Table S4: Elementally resolved total diffusion coefficients D_X and along the cartesian axes x , y , and z in $\times 10^8 \text{ cm}^2 \text{ s}^{-1}$ for $\text{CsPbBr}_x\text{I}_{3-x}$ structures with I_X at 700 K, for both an additional iodine and an additional bromine.

Interstitial					
in $\times 10^8 \text{ cm}^2 \text{ s}^{-1}$	D_{tot}	D_x	D_y	D_z	
Additional Iodine					
α -CsPbI ₃	30.3	30.1	30.0	30.7	
strained CsPbI ₃	29.0	30.6	28.3	28.1	
od-CsPbBr ₂ I	X=I	0.4	0.0	0.6	0.6
	X=Br	10.5	2.1	14.6	14.0
od-CsPbBrI ₂	X=I	5.2	2.5	5.7	7.2
	X=Br	0.0	0.0	0.0	0.0
Additional Bromine					
α -CsPbBr ₃	24.4	22.8	24.6	25.7	
strained CsPbBr ₃	24.1	21.7	21.6	28.9	
od-CsPbBr ₂ I	X=Br	10.2	3.1	18.1	12.0
	X=I	0.3	0.0	0.5	0.5
od-CsPbBrI ₂	X=Br	0.2	0.3	0.1	0.1
	X=I	6.0	3.5	6.7	7.8

Table S5: Elementally resolved total diffusion coefficients D_X and along the cartesian axes x , y , and z in $\times 10^9 \text{ cm}^2 \text{ s}^{-1}$ for $\text{CsPbBr}_x\text{I}_{3-x}$ structures with V_X at 700 K, for both a missing iodine and a missing bromine.

Vacancy					
in $\times 10^9 \text{ cm}^2 \text{ s}^{-1}$	D_{tot}	D_x	D_y	D_z	
Missing Iodine					
$\alpha\text{-CsPbI}_3$	9.7	8.9	9.2	11.0	
strained CsPbI_3	13.0	11.5	14.4	12.9	
od- CsPbBr_2I	X=I	20.0	0.0	35.5	24.1
	X=Br	0.0	0.0	0.1	0.1
od- CsPbBrI_2	X=I	14.1	13.9	12.3	16.1
	X=Br	0.0	0.0	0.0	0.0
Missing Bromine					
$\alpha\text{-CsPbBr}_3$	3.9	5.0	3.3	3.4	
strained CsPbBr_3	5.2	2.4	6.6	6.5	
od- CsPbBr_2I	X=Br	0.1	0.1	0.1	0.1
	X=I	23.8	0.2	31.7	40.2
od- CsPbBrI_2	X=Br	0.9	1.3	0.0	1.3
	X=I	13.6	15.9	12.1	12.9

2.1 Halide vacancy energy landscapes

In the following, we provide details on the procedure used to obtain site-dependent energies for halide vacancies in $\text{CsPbBr}_x\text{I}_{3-x}$, complementing the results presented in Tab. 3 in Section 3.2.2 of the main text. Site-dependent energies for halide vacancies were obtained by geometry optimization of all distinct vacancy positions in the $4\times 4\times 4$ supercell, using the same software and force field as the MD simulations. Each halide site in the pristine supercell was probed for the vacancy, yielding three symmetry-inequivalent positions per structure (Pb-Br, Pb-I, and Cs-Br/Cs-I), each with 64 equivalent instances. Prior to optimization, a short NVT -MD run of 1.25 ps at 500 K with a Berendsen thermostat ($\tau_T = 100$ fs) was performed to allow for local relaxation around the vacancy. Geometry optimizations were then carried out using a conjugate gradient algorithm (“Good” quality setting in AMS) at fixed cell volume. Reported energies are averages over all equivalent positions; error bars represent the standard error of the mean. In cases where the vacancy migrated to a neighboring layer during optimization, the displaced species was constrained to its initial neighboring-layer position. Results for a missing bromine are given in the main text; results for a missing iodine are given in Tab. S6.

Table S6: Relative total energies ΔE_{tot} of vacancy sites in CsPbBr_2I (± 0.03 eV) and CsPbBrI_2 (± 0.02 eV) for a missing iodine. Energies are referenced to the lowest-energy Pb-I site.

Missing I in: CsPbBr_2I		CsPbBrI_2	
Position	Total Energy (eV)	Position	Total Energy (eV)
Cs-Br	0.14	Cs-I	0.03
Pb-Br	0.14	Pb-Br	0.1
Pb-I	0	Pb-I	0

3 SI Note: Influence of strain

This section provides the full octahedral tilt pattern analysis for the layered and biaxially strained structures discussed in Section 3.1 of the main text, along with the procedure used to determine the target strain values. The rotation magnitude θ_{Mag} of the PbX_6 octahedra is derived from the complex conjugate eigenvalues of the rotation matrix, specifically $e^{i\theta_{\text{Mag}}}$ and $e^{-i\theta_{\text{Mag}}}$. A detailed analysis on the octahedral tilts can be found for CsPbBr_2I in Fig. S4 and for CsPbBr_2 in Fig. S5. There was strain applied to the pristine structures of $\alpha\text{-CsPbI}_3$ and $\alpha\text{-CsPbBr}_3$ in Fig. S6 to introduce octahedral tilting. The detailed analysis of those structures can be found for CsPbI_3 in Fig. S7 and for CsPbBr_3 in Fig. S8.

3.1 Layered Structures

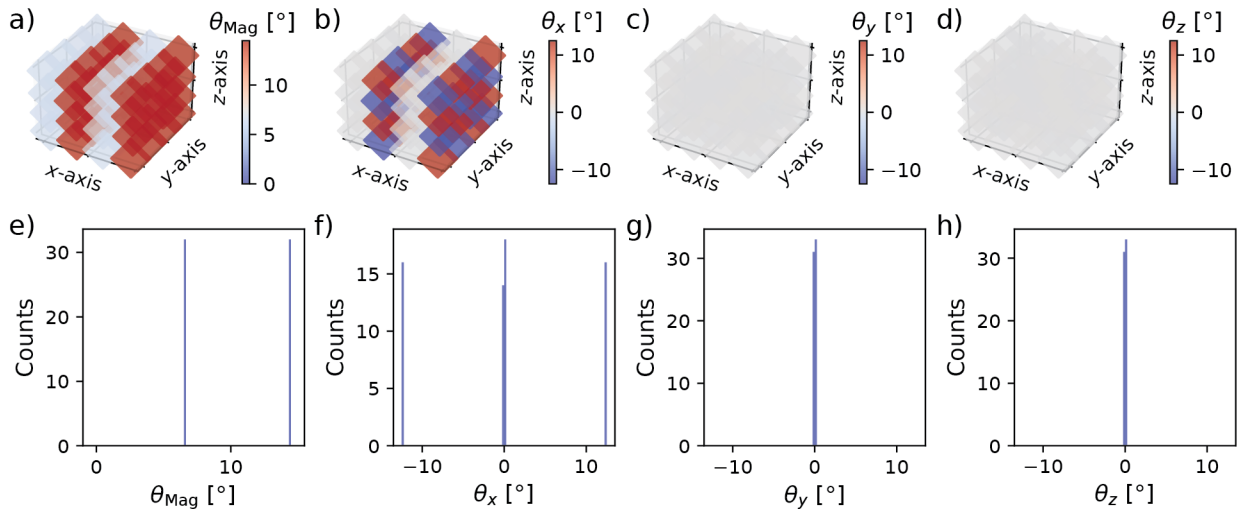


Figure S4: a) Time-averaged rotation magnitude of the PbX_6 octahedral tilts and b)-d) time-averaged tilt angles with respect to the cartesian axes ($\theta_x, \theta_y, \theta_z$) in layered $\text{CsPbBr}_2\text{I}_1$ perovskites. The color scale indicates the angle (in degrees) for each octahedron. Panel e)-h) are the histograms, referring to the respective pattern above, with 100 bins. The maxima are indicating different types of octahedrons. For Br octahedrons we observe $\theta_{\text{Mag}} \approx 6.6$, while $\theta_x, \theta_y, \theta_z \approx 0$, whereas for I octahedrons $\theta_{\text{Mag}} \approx 14.4$, while $\theta_y, \theta_z \approx 0$ and $\theta_x \approx \pm 12.4$.

Tilt directionality also shows a well-defined spatial pattern. Within the 2D Pb-X layers (parallel to the yz plane), we find a checkerboard-like alternating tilt pattern of θ_x in the Pb-I layers:

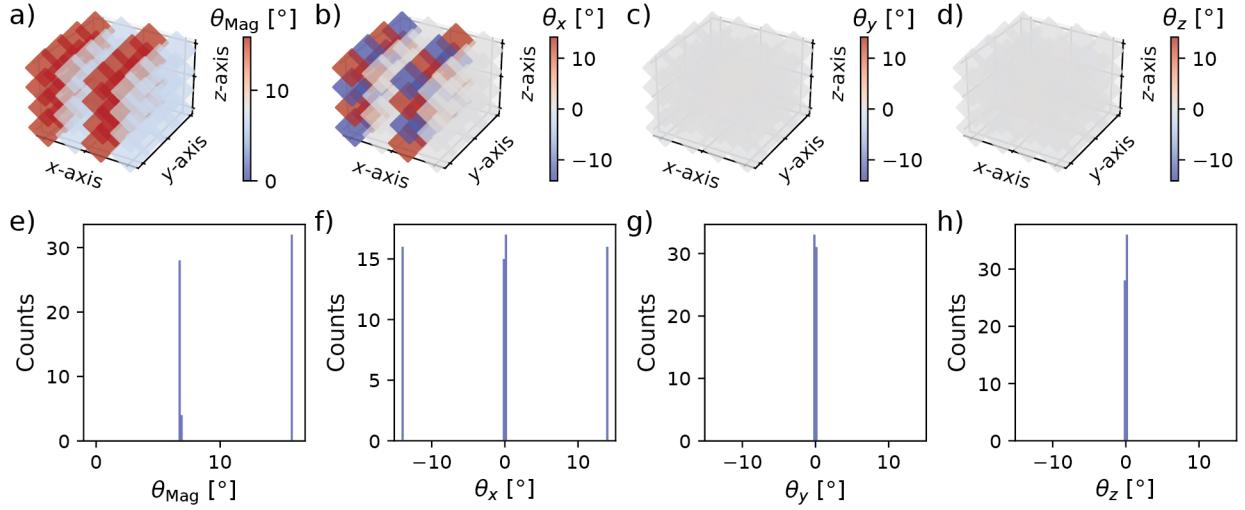


Figure S5: a) Time-averaged rotation magnitude of the PbX_6 octahedral tilts and b)-d) time-averaged tilt angles with respect to the cartesian axes ($\theta_x, \theta_y, \theta_z$) in layered $\text{CsPbBr}_2\text{I}_1$ perovskites. The color scale indicates the angle (in degrees) for each octahedron. Panel e)-h) are the histograms, referring to the respective pattern above, with 100 bins. The maxima are indicating different types of octahedrons. For Br octahedrons we observe $\theta_{\text{Mag}} \approx 6.8$, while $\theta_x, \theta_y, \theta_z \approx 0$, whereas for I octahedrons $\theta_{\text{Mag}} \approx 15.8$, while $\theta_y, \theta_z \approx 0$ and $\theta_x \approx \pm 14.0$

individual octahedra are tilted, such that every octahedron is surrounded in all in-plane directions by neighbors tilted in the opposite sense. The tilt around the y - and z -axes as well as the magnitude of the octahedral tilts and all angular components in the Pb-Br layers are close to zero, indicating a clear confinement of the distortion to the strained layers.

3.2 Applied biaxial strain to pristine α - CsPbBr_3 and α - CsPbI_3

To assess whether strain alone can reproduce the characteristic octahedral tilts observed in the layered structures, biaxial compression was applied in the yz -plane to chemically homogeneous α - CsPbI_3 , whereas biaxial tension was applied to α - CsPbBr_3 . The out-of-plane (x) lattice parameter was held fixed at 23.83 Å for CsPbBr_3 and 25.53 Å for CsPbI_3 throughout. Compressive (tensile) stress along the y - and z -directions was applied using the same ReaxFF force field of Ref. 1.

For each stress value, the following procedure was applied. A fresh supercell was pre-relaxed with a short NVT -MD run of 1.25 ps at 700 K. The cell was then compressed (CsPbI_3) or expanded (CsPbBr_3) equally in the y - and z -directions via a geometry optimization with only the

x -dimension fixed, using a stress tensor of the form $[0, p, p, 0, 0, 0]$. Stress was varied over 50 steps from 1 to 30000 atm for CsPbI₃ and from -1 to -30000 atm for CsPbBr₃. The resulting cell dimensions were then used as input for a 7.5 ps *NVT*-MD run (output frequency 0.5 ps), of which the final 5 ps were used for the tilt analysis. To account for fluctuations in volume and tilt, the entire procedure was repeated three times per stress value and results were averaged. The target geometry for the production MD runs was selected as the lowest-strain configuration that reproduced the approximate $\theta_x:\theta_y:\theta_z$ ratio of the layered od-structures while maintaining structural stability.

For the MD simulations in strained systems, we fixed the dimensions of CsPbBr₃: 23.83x24.2x24.2 Å, and CsPbI₃: 25.53x24.52x24.52 Å. This achieved moderate strain in the yz plane to achieve the desired tilt patterns, while still maintaining the stability of the structures in longer MD runs. For enhanced visibility of the tilt patterns, we used the most strongly compressed volume for CsPbI₃ and the strongest stable inflation of CsPbBr₃ for the following figures.

As expected, the strained CsPbI₃-structure in Fig. S7 lacks the layered modulation of tilt magnitude seen in mixed-halide systems, since it is fully homogeneous and does not contain Br-rich regions. Thus, while the checkerboard pattern emerges, it is no longer separated by undistorted layers. Additionally, the tilt components perpendicular to the layers (x -direction), while still smaller than the in-plane components, are non-zero, in contrast to the strictly planar confinement seen in the layered architecture.

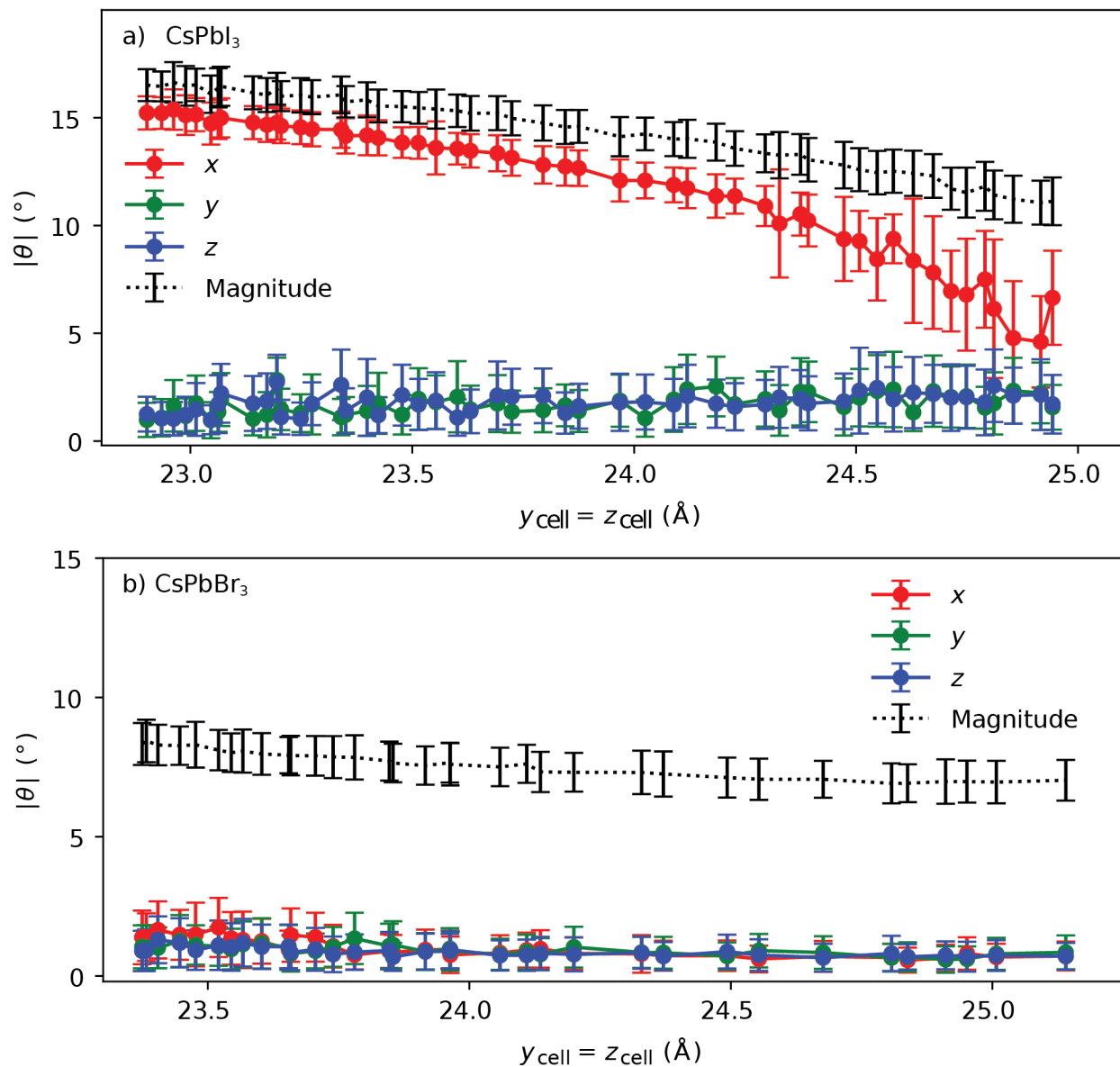


Figure S6: The supercell vectors $y_{\text{cell}} = z_{\text{cell}}$ vs. the absolute tilt $|\theta|$ for a) CsPbI_3 under compressive stress and $x_{\text{cell}} = 25.53 \text{ \AA}$; b) CsPbBr_3 under tensile stress and $x_{\text{cell}} = 23.83 \text{ \AA}$. The target volumes for achieving the desired tilt patterns are highlighted.

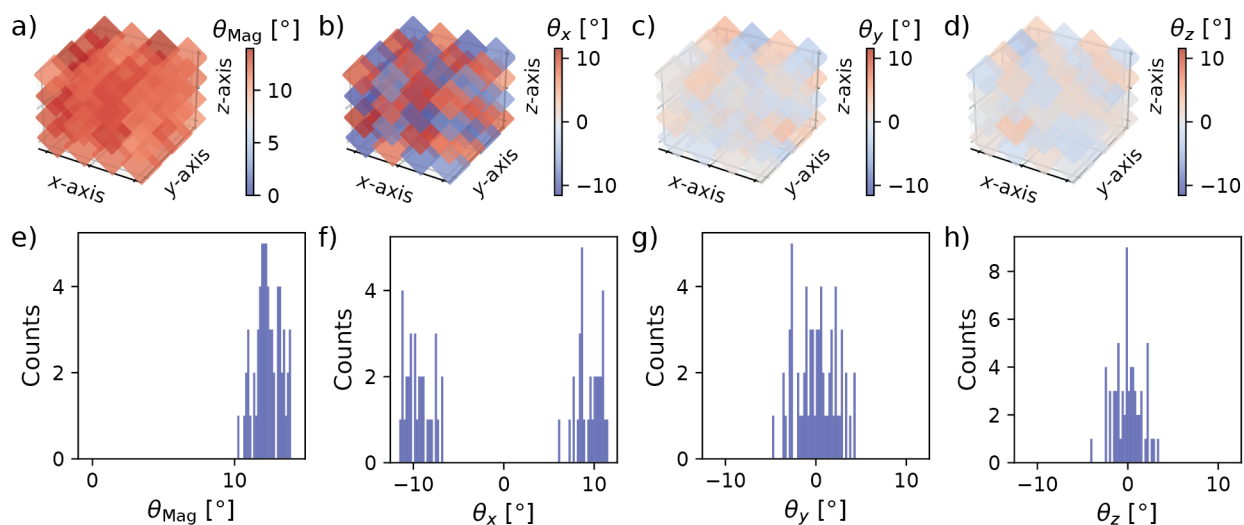


Figure S7: a) Time-averaged rotation magnitude of the PbX_6 octahedral tilts and b)-d) their components along the axes in CsPbI_3 under biaxial compression to achieve similar tilt magnitudes as in layered $\text{CsPbBr}_2\text{I}_1$. The color scale indicates the angle (in degrees) for each octahedron. Panel e)-h) are the histograms, referring to the respective pattern above, with 100 bins. We observe $\theta_{\text{Mag}} \approx 12.6$, while $\theta_y, \theta_z \approx 0$ and $\theta_x \approx \pm 9.3$

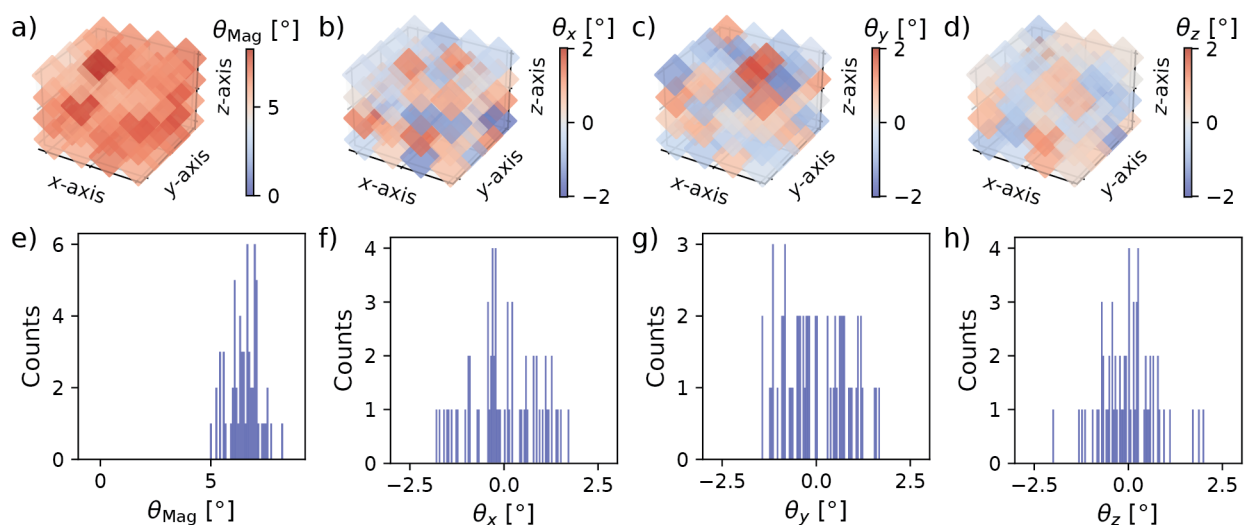


Figure S8: a) Time-averaged rotation magnitude of the PbX_6 octahedral tilts and b)-d) their components along the axes in CsPbBr_3 under biaxial compression to achieve similar tilt magnitudes as in layered $\text{CsPbBr}_2\text{I}_1$. The color scale indicates the angle (in degrees) for each octahedron. Panel e)-h) are the histograms, referring to the respective pattern above, with 100 bins. We observe $\theta_{\text{Mag}} \approx 6.7$, while $\theta_x, \theta_y, \theta_z \approx 0$.

References

- (1) Pols, M.; van Duin, A. C. T.; Calero, S.; Tao, S. Mixing I and Br in Inorganic Perovskites: Atomistic Insights from Reactive Molecular Dynamics Simulations. *J. Phys. Chem. C* **2024**, *128*, 4111–4118.